Two-dimensional and surface backscattering Mueller matrices of anisotropic sphere-cylinder scattering media: a quantitative study of influence from fibrous scatterers

Honghui He
Nan Zeng
E. Du
Yihong Guo
Dongzhi Li
Ran Liao
Yonghong He
Hui Ma

Two-dimensional and surface backscattering Mueller matrices of anisotropic sphere-cylinder scattering media: a quantitative study of influence from fibrous scatterers

Honghui He,a Nan Zeng,a E. Du,a,b Yihong Guo,a,b Dongzhi Li,a,b Ran Liao,a Yonghong He,a and Hui Maa,b
aTsinghua University, Graduate School at Shenzhen, Shenzhen Key Laboratory for Minimal Invasive Medical Technologies, Shenzhen 518055, China
bTsinghua University, Department of Physics, Beijing 100084, China

Abstract. We present both the two-dimensional backscattering point-illumination and surface-illumination Mueller matrices for the anisotropic sphere-cylinder scattering media. The experimental results of the microsphere-silk sample show that the Mueller matrix elements of an anisotropic scattering medium are different from those of an isotropic medium. Moreover, both the experiments and Monte Carlo simulations show that the directions of the fibrous scatterers have prominent effects on the Mueller matrix elements. As the fibrous samples rotate, the surface-illumination Mueller matrix measurement results for the m12, m21, m13, m31, m22, m23, m32, and m33 elements represent periodical variations. Experiments on skeletal muscle and porcine liver tissue samples confirm that the periodical changes for the surface-illumination Mueller matrix elements are closely related to the well aligned fibrous scatterers. The m22, m23, m32, and m33 elements are powerful tools for quantitative characterization of anisotropic scattering media, including biological tissues. © 2013 Society of Photo-Optical Instrumentation Engineers (SPIE) [DOI: 10.1117/1.JBO.18.4.046002]

Keywords: Mueller matrix; scattering; polarization; tissue; anisotropy.

Paper 12807R received Dec. 19, 2012; revised manuscript received Mar. 11, 2013; accepted for publication Mar. 14, 2013; published online Apr. 1, 2013; corrected Apr. 4, 2013.

1 Introduction

Polarization measurement is a powerful tool to probe the fundamental interactions between photons and media. To describe the polarization states of photons and the properties of media, different representations have been established. For turbid media, the Stokes vector–Mueller matrix method is applicable because of its capability for quantitatively describing the behaviors of both the completely polarized and partially depolarized scattered photons.[1] It has been demonstrated in previous publications, that for an isotropic medium, one may obtain the density and sizes of the scatterers from the two-dimensional (2-D) patterns of backscattering Mueller matrix when the illumination spot is much smaller than the imaging area.[2–4] However, for light scattering in more complicated anisotropic turbid media,[5–9] it is not trivial to carry out such a quantitative analysis of the Mueller matrix elements. Each element may correlate to different properties of the media, making it difficult to find explicit relations between the two.[10] Thus, there have been strong motivations to interpret the physics insights hidden within the Mueller matrix. Recently, a method called polar decomposition of Mueller matrix has been developed to separate different contributions by scattering, retardation and dichroism,[11] and tested in biomedical applications.[12–20]

Most biological tissues contain structurally anisotropic components, such as the myofibrils in skeletal muscles, the collagen fibers in tendons, and axon.[21,22] For the studies of biomedical optics and its applications in therapeutics and diagnostics, one needs to use properly simplified models to understand the complicated interactions between photons and the anisotropic biological tissues, and to extract the structural information of the sample. In previous studies we have used the sphere-cylinder scattering model (SCSM) to explain the polarized optical properties of biological tissues, including skeletal muscles.[23–26] On the other hand, we have demonstrated that the Mueller matrix can be used to characterize the properties of a sphere-cylinder scattering medium.[10] In this paper, we measure and compare both the 2-D backscattering Mueller matrix patterns and the surface-illumination Mueller matrix for the anisotropic sphere-cylinder scattering media. We examine in detail the characteristic features in each Mueller matrix element and the influence of the fibrous scatterers on the Mueller matrix. Moreover, the experimental and Monte Carlo simulated results show that the Mueller matrix elements can be used to characterize the structural properties of some anisotropic biological tissues. Combined with other quantitative techniques, such as polar decomposition and rotating linear polarization imaging (RLPI),[13,25] the Mueller matrix and SCSM can be used as potentially powerful tools in biomedical applications including pathological diagnosis.

2 Materials and Methods

2.1 Experimental Setup

In this paper, two types of experimental setups are used; one is a typical configuration for 2-D backscattering Mueller matrix pattern measurements, as shown in Fig. 1(a).[27,28] The light source is a 633-nm linearly polarized He-Ne laser. The polarization states of the incident light are controlled by a set of a quarter-wave
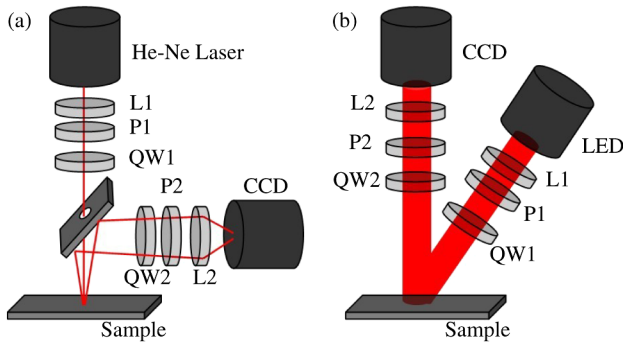
Fig. 1 Schematics of the experimental setups. *P*: polarizer; *QW*: quarter-wave plate; *L*: lens. (a) Setup for the 2-D backscattering Mueller matrix pattern measurement. The diameter of the illumination area from the He-Ne laser is about 1 mm, which is smaller than the imaging area (about 1.5 × 1.5 cm). (b) Setup for the surface-illumination Mueller matrix measurement. The polarized light illuminates the sample at about 30 deg angle to the normal to minimize the surface reflection effects. The diameter of the illumination area from the LED is about 2 cm, which is larger than the imaging area (about 1.5 × 1.5 cm).

plate (QW1) and a linear polarizer (P1). A mirror with a front surface tilted at a 45-deg angle to the normal is positioned in front of the sample. The incident light reaches the sample through a 5-mm hole at the center of the mirror. Reflection from the sample surface is directed to pass through the same hole to minimize its interference to the back reflected light. The reflection polarization states are controlled by a second

set of a quarter-wave plate (QW2) and linear polarizer (P2). Then the backscattering photons are steered to and recorded by a 14-bit CCD camera to produce the reflectance images of the samples. In this part of experiments, the illumination area from the He-Ne laser is confined to a 1-mm spot, which is much smaller than the imaging area (1.5 × 1.5 cm). Then, we can obtain the patterns of the backscattering Mueller matrix elements for a turbid medium.

The other experimental setup used in this paper is for surface-illumination Mueller matrix measurement, as shown in Fig. 1(b).[29–34] Compared to Fig. 1(a), the main difference of this configuration is the illumination method. The diameter of the illumination area for Fig. 1(b) is about 2 cm, which is larger than the sample or the imaging area (1.5 × 1.5 cm). Therefore, the scattering patterns are smoothed out in the surface backscattering Mueller matrix. Instead, the intensity matrix elements for the samples are obtained. To eliminate the reflection from the sample's surface, the polarized light from a 1 W light emitting diode (LED) illuminates the sample at about a 30-deg angle to the normal. For measuring the 4 × 4 Mueller matrix, six polarization states for the incident light are achieved, i.e., horizontal linear (*H*), vertical linear (*V*), 45-deg linear (*P*), 135-deg linear (*M*), left circular (*L*), and right circular (*R*), then, six polarization components corresponding to each incident state are measured. After a total of 36 measurements are conducted, the Mueller matrix of a turbid scattering medium can be calculated as Eq. (1):

$$
\begin{aligned}
M &= \begin{pmatrix} m11 & m12 & m13 & m14 \\ m21 & m22 & m23 & m24 \\ m31 & m32 & m33 & m34 \\ m41 & m42 & m43 & m44 \end{pmatrix} \\
&= \frac{1}{2} \begin{pmatrix} HH+HV+VH+VV & HH+HV-VH-VV & PH+PV-MP-MM & RH+RV-LH-LV \\ HH-HV+VH-VV & HH-HV-VH+VV & PH-PV-MH+MV & RH-RV-LH+LV \\ HP-HM+VP-VM & HP-HM-VP+VM & PP-PM-MP+MM & RP-RM-LP+LM \\ HR-LL+VR-RL & HR-VR+VL-HL & PR-MR+ML-PL & RR-RL-LR+LL \end{pmatrix}.
\end{aligned}
\tag{1}
$$

2.2 Sample and Monte Carlo Program

In this paper, a microsphere-silk sample for the SCSM is designed and measured. It is a 5 × 2.8 × 2 cm cube consisting of three layers.[10] The first and third layers are solutions of polystyrene microsphere (International Laboratory, USA), and the second layer is a 3-mm thickness slab of well-aligned silk fibers. For the polystyrene microsphere solution, the diameter of the microsphere is 0.2 μm, and the total scattering coefficient of the solution is 5 cm^{-1}. The parameters of the silk fiber layer were determined in the previous study.[24] The diameter of the silk fiber is taken as 1.5 μm, and the refractive index is 1.56. The scattering coefficient of the silk layer is estimated as 70 cm^{-1}. During the experiments, the direction of the silk layer has been adjusted to vary the anisotropy axis. To examine the relationship between the Mueller matrix and the microscopic structure of the sample, the experimental results are compared to Monte Carlo simulations based on the SCSM developed in our previous work.[24] For the SCSM, the anisotropic and isotropic microstructures in the sample are approximated as a mixture

of infinitely long cylindrical and spherical scatterers embedded in a surrounding medium. In this paper, we use the simple SCSM, which consists of single dispersed spheres and cylinders immersed in an isotropic medium. The parameters used in the Monte Carlo simulations are set to be the same as the experiments. The diameters of spherical and cylindrical scatterers are 0.2 and 1.5 μm, respectively, and the refractive indices are 1.59 and 1.56, respectively. The refractive index of the surrounding medium is 1.33. The standard deviation of angular distribution of the cylinders is 10 deg. The scattering coefficients of the spherical and cylindrical scatterers are 5 and 70 cm^{-1}, respectively.

3 Results and Discussion

3.1 Experimental Results of Mueller Matrices for Sphere-Cylinder Scattering Samples

The experimental results of the backscattering Mueller matrices for the sphere-cylinder scattering medium are shown in Fig. 2
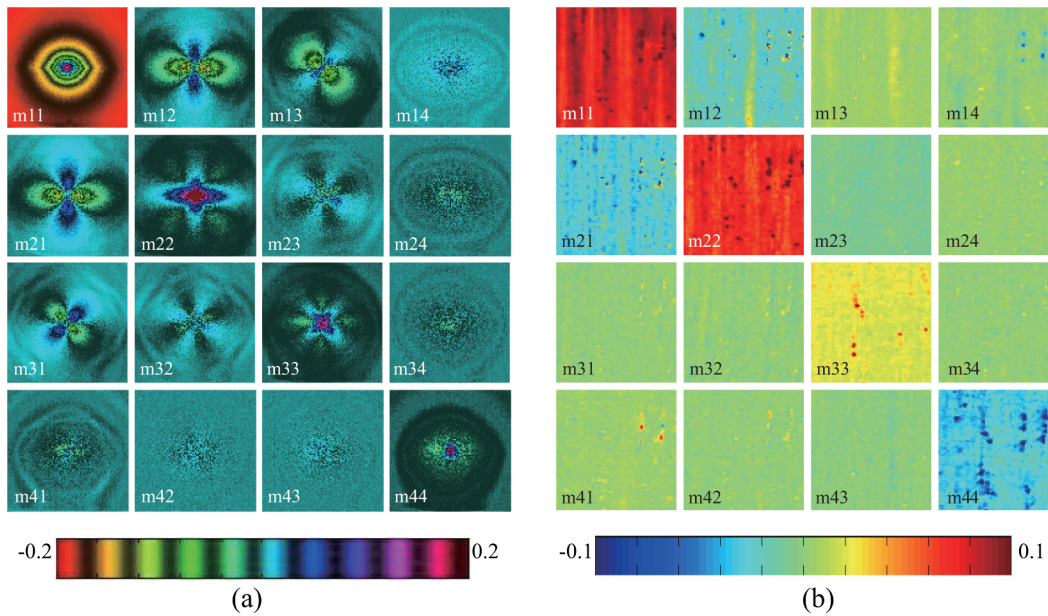
Fig. 2 Experimental results of the backscattering Mueller matrices for the samples containing silk fibers and spheres. The silk fibers are along the y-axis direction: (a) 2-D backscattering Mueller matrix patterns; (b) intensity values for the surface-illumination Mueller matrix measurements. All the Mueller matrix elements are normalized by the m11 element. Please note that m11 uses its own colormap from 0 to 1, and the colormap for m22 and m33 in (b) is from −0.3 to 0.3.

[Fig. 2(a) shows the 2-D backscattering Mueller matrix patterns, and Fig. 2(b) shows the intensity for the surface-illumination Mueller matrix measurements]. In Fig. 2, the silk fibers are distributed along the y-axis direction. Comparing to the Mueller matrix of an isotropic scattering medium (as shown in Fig. 3), the characteristic features of the 2-D backscattering Mueller matrix patterns for the SCSM can be summarized as follows: The m11 element for the isotropic medium is always circular. However, for the sphere-cylinder scattering medium, the m11 is rhombic. The rhombic shape is a unique feature for the existence of anisotropic scattering.[10]

The m12 and m21 elements are quatrefoils for both the isotropic and sphere-cylinder scattering media, with negative value around the x axis and positive value around the y axis. For the isotropic medium, the intensity around the x axis is the same as that around the y axis [Fig. 3(a)]. However, for the sphere-cylinder medium with the cylinders along the y axis direction, the intensity around the x axis becomes higher. The m13 and m31 elements are also quatrefoils, with a 45-deg rotation to the m12 and m21 elements. For both the isotropic and anisotropic scattering media, the intensity distributions around the x and y axes are the same. In an isotropic medium, the total intensities and sizes of the m13 and m31 elements are nearly the same as the m12 and m21 elements, but for the anisotropic medium with y axis direction cylinders, and the total intensities of the m13 element, m31 becomes lower than the m12 and m21 elements. The m22 element has a cross-like pattern. For the isotropic medium, the intensity distributions around x and y axes are close. However, in the sphere-cylinder scattering medium, the intensity around the x axis is higher than that around the y axis. The m33 element always has a cross-like pattern, which is similar to the m22 element with a 45-deg rotation, but the intensity distributions around the 45 deg- and 135-deg axes are close. In the sphere-cylinder medium with the fibrous scatterers along the y axis, the total intensity of the m33 element

become lower than the m22 element. The m23 and m32 elements have similar patterns. In the sphere-cylinder scattering medium, the intensity around the x axis is slightly larger than that in other parts. The m14, m41, m24, m42, m34, and m43 elements in the isotropic medium with small spherical scatterers are blanks, but for the sphere-cylinder medium, these elements may have some slight residue intensity along the x axis. The m44 elements for the isotropic and sphere-cylinder scattering media have circular patterns.

It should be pointed out that, for a sphere-cylinder scattering medium containing larger spherical scatterers, the 2-D Mueller matrix patterns are slightly different. For instance, the m24, m42, m34, and m43 elements may have clearer patterns. However, the main characteristic features are similar. For the sphere-cylinder scattering medium, the Mueller matrix patterns can be considered as the contributions from both the spherical and cylindrical scatterers. According to the Mie scattering theory for infinitely long cylinders, the photons tend to be scattered to the perpendicular direction of cylindrical scatterers,[1] i.e., the x axis in Fig. 2(a). Therefore, for most matrix elements in Fig. 2(a), the intensity distributions along the x axis are larger than that in other parts. Using the property of the matrix elements, the relative concentration of the cylindrical scatterers can be decided.

All the characteristic features for the 2-D patterns mentioned above can be used to detect the cylindrical scatterers in a turbid media. However, the 2-D backscattering Mueller matrix patterns can only be easily and clearly obtained for homogeneous scattering media, such as the solutions with well-aligned fibers. For inhomogeneous media, the surface-illumination Mueller matrix measurements are more suitable. Since the illumination area is larger than the imaging area for the surface Mueller matrix measurements, the patterns as shown in Figs. 2(a) and 3(a) are no longer existed. What we get in the surface-illumination Mueller matrix measurement is an intensity matrix, as shown in Fig. 2(b)
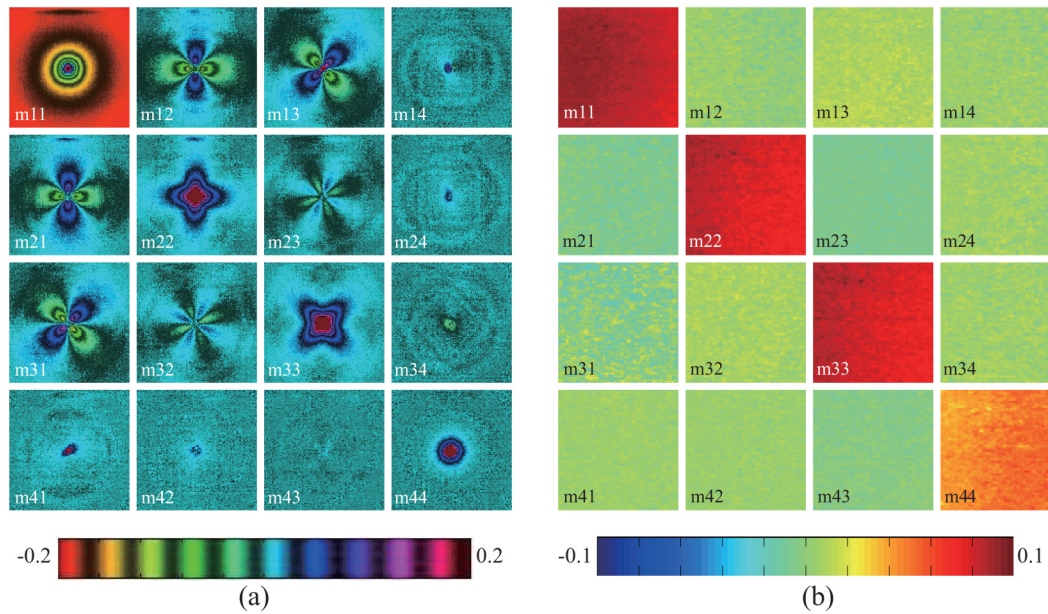
Fig. 3 Experimental results of the backscattering Mueller matrices for the medium containing only 0.2-μm spherical scatterers: (a) 2-D backscattering Mueller matrix patterns; (b) intensity values for the surface-illumination Mueller matrix measurements. All Mueller matrix elements are normalized by m11. Please note that m11 uses its own colormap from 0 to 1, and the colormap for m22 and m33 in (b) is from −0.3 to 0.3.

for the same microsphere-silk sample with the fibers along the y-axis direction. Comparing to the results of an isotropic scattering medium [Fig. 3(b)], the characteristic features for the sphere-cylinder medium are different. For an isotropic medium [Fig. 3(b)], the Mueller matrix is diagonal, and the m12, m13, m14, m21, m23, m24, m31, m32, m34, m41, m42, and m43 elements are blanks. This is because that the quatrefoil patterns shown in Fig. 3(a) with both positive and negative parts will be smoothed out when the illumination area is larger than the imaging plane. Moreover, the m22 and m33 elements are equal, and their values are positive. The values of the m22, m33, and m44 elements are closely related to the particle sizes of isotropic media. As the diameter of the particles increases, the intensities of m22 and m33 decrease. However, for the sphere-cylinder medium [as shown in Fig. 2(b)], the off-diagonal elements are no longer zeros, and the total intensity values for the m22 and m33 elements become different. For the sample containing silk fibers along the y axis, m12 and m21 are negative. Moreover, the value for m22 is much larger than m33. These intensity changes can be explained by using the 2-D backscattering Mueller matrix patterns, as shown in Fig. 2(a). The cylinders along y axis results in more photons to be scattered to the x-axis direction; therefore, the negative parts become larger than the positive parts for the m12 and m21 elements. Meanwhile, the pattern of the m22 element becomes more prominent than the m33 element, resulting in higher value of m22 than m33 in Fig. 2(b).

3.2 Influence of Direction of the Fibers on the Mueller Matrices

To analyze the influence of the direction of the fibers on the Mueller matrix elements, we rotate the silk layer of the sample. Figures 4(a) and 5(a) show the 2-D patterns for the samples with silks along the x- and 45-deg-axes directions, respectively. Compared to Fig. 2(a), the elongation directions for the rhombic m11 elements are changed to the y and 135-deg axes,

respectively. Hence, the elongation of m11 can be used to decide the direction of the cylinders. According to the Mie scattering theory, for the cylindrical scatterers along the x-axis direction, photons tend to be scattered to y axis. Therefore, in Fig. 4(a), the positive parts for the m12 and m21 elements become prominent, and the m22 becomes larger than the m33, with both patterns rotated by 90 deg as compared to Fig. 2(a). The elements in the fourth row and fourth column have no clear patterns. For the cylindrical scatterers along the 45-deg-axis direction, photons tend to be scattered to the direction along the 135-deg axis. Hence, for the m13 and m31 elements with quatrefoil shapes in Fig. 5(a), the positive intensity around the 135-deg axis is higher. The m12 and m21 elements are also quatrefoils, whose total intensities and sizes become lower than the m13 and m31 elements. Meanwhile, the m22 element still has a cross-like pattern, but compared to Fig. 2(a), the intensity distributions around the x and y axes are getting much closer. The m33 element becomes much larger than m22, and the intensity along the 135-deg axis is more prominent than those along other directions.F

Figures 4(b) and 5(b) show the surface-illumination Mueller matrix intensities for the samples, in which the silk fibers are along the y axis and 135-deg axes, respectively. It is clearly shown that as the rotation of the silk fibers, the total values of m11, and the elements in the fourth row and fourth column are not affected. However, the other elements represent periodical intensity changes. For the sample with the silk layer along the 45-deg axis, the values of the m13 and m31 elements are positive, while m12 and m21 are blanks (Fig. 6). What is more, the value of the m22 becomes much smaller than that of the m33 element. Meanwhile, when the silk fibers are rotated to the x-axis or y-axis directions, the m12 and m21 elements become positive or negative, respectively, while the values of m13 and m31 become zeros. Moreover, the value of m22 is larger than m33. Such periodical variations do not exist in isotropic media. Further analysis based on the experimental and Monte Carlo simulations show that the variation period for
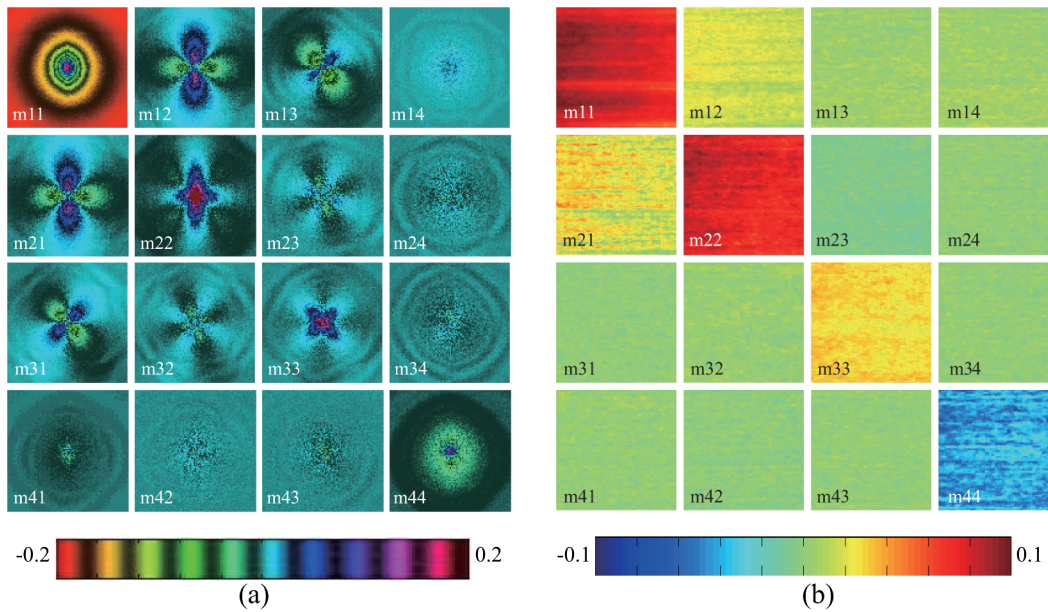
Fig. 4 Experimental results of the backscattering Mueller matrices for the sphere-cylinder scattering model (SCSM) medium. The silk fibers are along the *x*-axis direction: (a) 2-D backscattering Mueller matrix patterns; (b) intensity values for the surface-illumination Mueller matrix measurements. All Mueller matrix elements are normalized by m11. Please note that m11 uses its own colormap from 0 to 1, and the colormap for m22 and m33 in (b) is from −0.3 to 0.3.
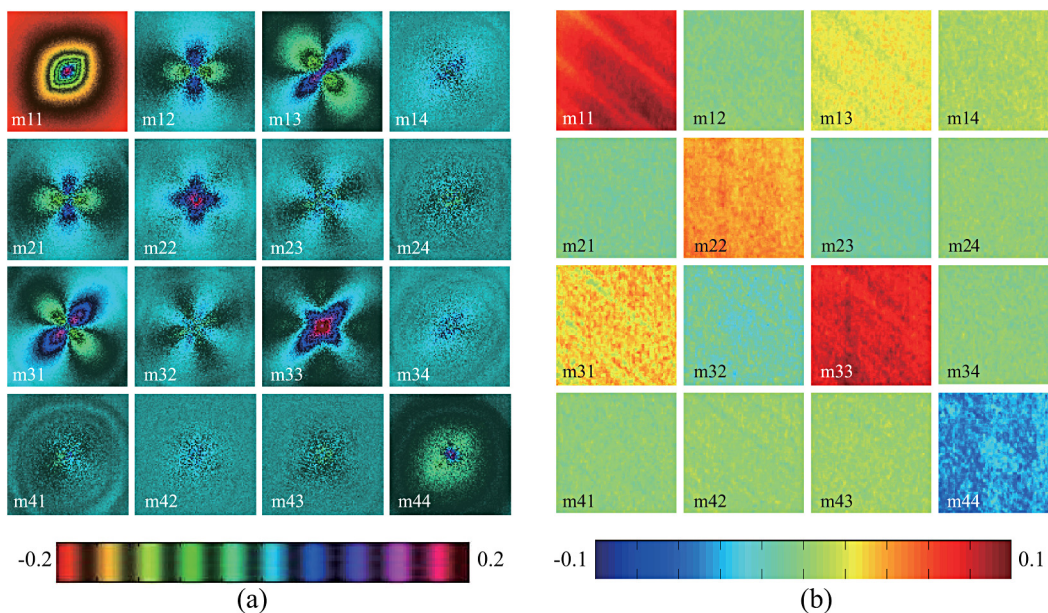

Fig. 5 Experimental results of the backscattering Mueller matrices for the sphere-cylinder scattering model (SCSM) medium. The silk fibers are along the 45-deg axis direction: (a) 2-D backscattering Mueller matrix patterns; (b) intensity values for the surface-illumination Mueller matrix measurements. Please note that m11 uses its own colormap from 0 to 1, and the colormap for m22 and m33 in (b) is from −0.3 to 0.3.

the m22, m23, m32, and m33 elements is π [as shown in Fig. 7 (b), 7(c), 7(e), and 7(f)], while that for m12, m13, m21, and m31 is 2π [as shown in Fig. 7(a) and 7(d)]. The m22 element represents the ability for the medium to maintain horizontal (H) or vertical (V) linear polarization states at H or V polarized incidence. The m33 element represents the ability to maintain 45-deg linear (P) or 135-deg linear (M) polarization components at P or M polarized incidence. The m23 and m32 elements represent the medium's ability to change P and M (or H and

V) linear polarization states to H and V (or P and M) states. The m22, m23, m32, and m33 elements have much larger amplitudes than those for the m12, m13, m21, m31 elements. All these intensity changes can be explained by using the 2-D Mueller matrix patterns and Mie scattering theory for infinitely cylinders, as discussed above. It can also be observed in Fig. 7 that the Monte Carlo simulations regenerate the dominant features of the experiments. The discrepancies between the experiments and simulations, which are particularly prominent for
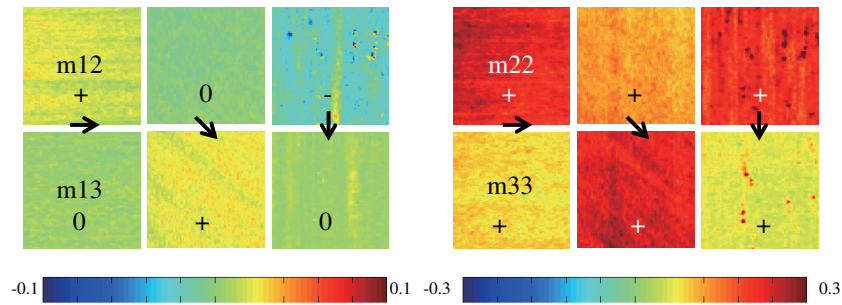
Fig. 6 The surface-illumination Mueller matrix measured m12, m13, m22, and m33 elements for the samples with the silk fibers along the x- (left), 45-deg (middle), and y-axes (right) directions. The arrows represent the directions of the silk fibers.
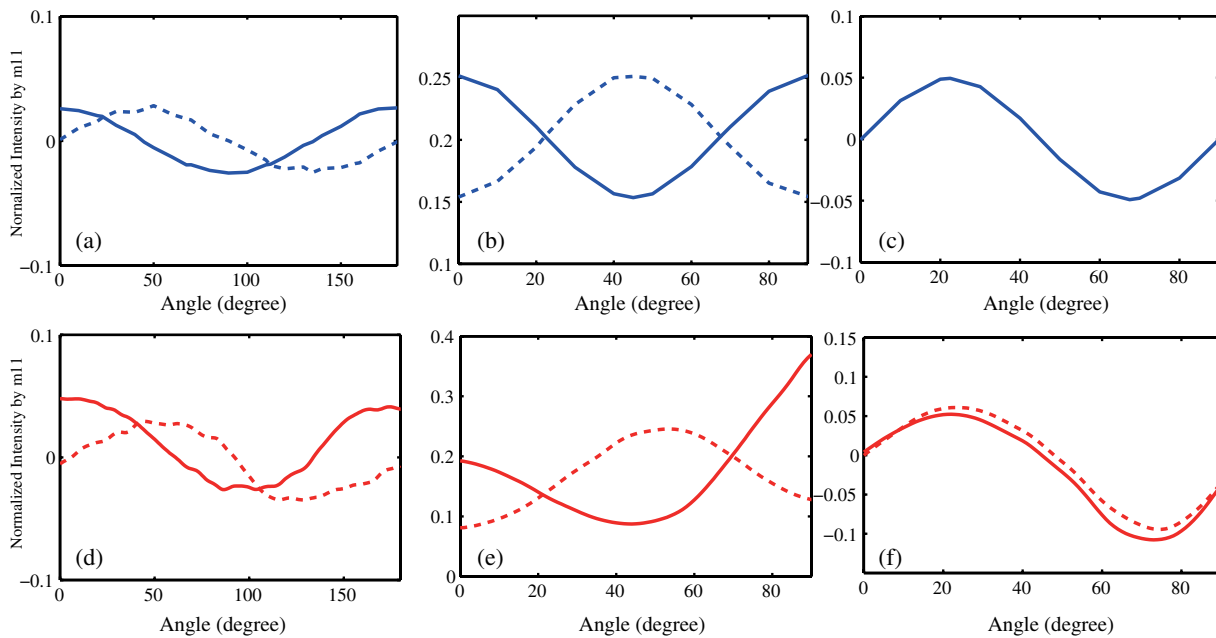

Fig. 7 Dependence of average values of surface-illumination Mueller matrix elements to the directions of the silk fibers. Comparison between simulated results (upper blue lines) and experiments (bottom red lines). (a) and (d): m12 (solid lines) and m13 (dash lines); (b) and (e): m22 (solid lines) and m33 (dash lines); (c) and (e): m23 (solid lines) and m32 (dash lines). All the elements are normalized by m11. The parameters used in Monte Carlo simulation match the experiments.
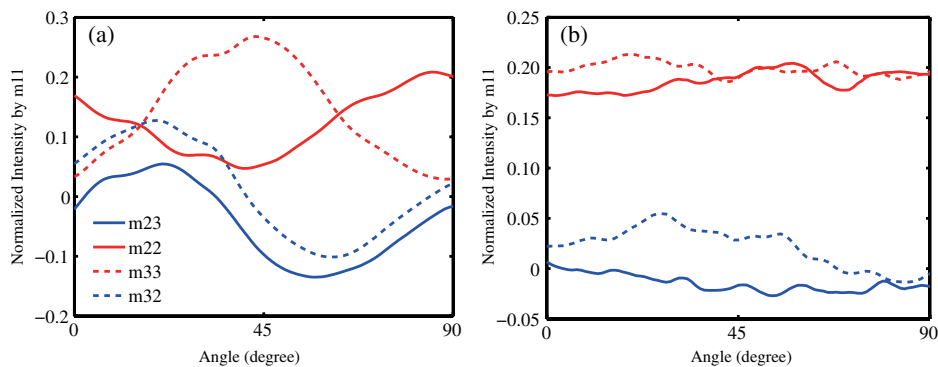

Fig. 8 Dependence of the surface-illumination Mueller matrix average values of the m23, m22, m33, and m32 elements to the directions of the biological samples: (a) fresh bovine skeletal muscle sample; (b) porcine liver tissue sample.

m22 and m33, are resulted from the oblique incidence in current experimental configuration.

3.3 Measurements of Biological Tissues

The periodical variations of the surface-illumination Mueller matrix elements can also be observed for the anisotropic biological tissue (Fig. 8). The tissue sample is a cube of fresh bovine skeletal muscle.[35] In the experiments, the muscle fibers are aligned parallel to the imaging $x - y$ plane. Then, we rotate the muscle sample to vary the direction of the muscle fibers from 0 deg to 90 deg. As shown in Fig. 8(a), the m22, m23, m32, and m33 elements represent periodical variations similar to Fig. 7. For comparison, we also measured the Mueller matrix elements for an isotropic porcine liver tissue, as shown in Fig. 8(b). It can be observed that, with the rotation of the liver sample, the intensities of the m22, m23, m32, and m33 elements represent no such periodical change, as shown in Fig. 8(a). Further experiments and Monte Carlo simulations based on SCSM show that the periodical variations are characteristic features for anisotropic scattering media. The amplitude of the variation is closely related to the magnitude, or degree, of anisotropy. Moreover, the values of the m22 and m33 elements are sensitive to the sizes of the scatterers.

4 Conclusion

In summary, we measured and compared both the 2-D backscattering Mueller matrix patterns and the surface-illumination Mueller matrix for the anisotropic sphere-cylinder scattering media. The experimental results show that the Mueller matrix of an anisotropic scattering medium is distinctively different from that of an isotropic medium. The 2-D Mueller matrix patterns contain a large amount of information for the anisotropic scattering media; however, the patterns can only be clearly obtained for homogeneous scattering media. For inhomogeneous media, including some biological tissues, the surface-illumination Mueller matrix measurements are more suitable. Both the experiments and Monte Carlo simulations show that the directions of the fibrous scatterers have prominent effects on the Mueller matrix elements. Particularly, as the fibrous structures rotate, the intensities of the m12, m21, m13, m31, m22, m23, m32, and m33 elements of the surface-illumination Mueller matrix display periodical variations, which do not exist for isotropic scattering media. Using the amplitude of the variations, the anisotropic degree can be examined. In addition, the experiments using the bovine skeletal muscle and porcine liver tissue samples confirm that the periodical changes for the Mueller matrix elements are closely related to the fibrous scatterers. The m22, m23, m32, and m33 elements are powerful tools to develop a quantitative method for characterization of anisotropic scattering media including biological tissues.

References

1. C. F. Bohren and D. R. Huffman, *Absorption and Scattering of Light by Small Particles*, John Wiley and Sons, New York (1983).
2. B. D. Cameron, Y. Li, and A. Nezhuvingal, "Determination of optical scattering properties in turbid media using Mueller matrix imaging," *J. Biomed. Opt.* **11**(5), 054031 (2006).
3. Y. Deng et al., "Numerical study of the effects of scatterer sizes and distributions on multiple backscattered intensity patterns of polarized light," *Opt. Lett.* **33**(1), 77–79 (2008).
4. Y. Deng et al., "Characterization of backscattering Mueller matrix patterns of highly scattering media with triple scattering assumption," *Opt. Express* **15**(15), 9672–9680 (2007).
5. I. S. Nerbo et al., "Real-time in situ Mueller matrix ellipsometry of GaSb nanopillars: observation of anisotropic local alignment," *Opt. Express* **19**(13), 12551–12561 (2011).
6. I. S. Nerbo et al., "Characterization of inclined GaSb nanopillars by Mueller matrix ellipsometry," *J. Appl. Phys.* **108**(1), 014307 (2010).
7. A. Kienle, F. K. Forster, and R. Hibst, "Anisotropy of light propagation in biological tissue," *Opt. Lett.* **29**(22), 2617–2619 (2004).
8. A. Kienle and R. Hibst, "Light guiding in biological tissue due to scattering," *Phys. Rev. Lett.* **97**(1), 018104 (2006).
9. A. Shuaib and G. Yao, "Equi-intensity distribution of optical reflectance in a fibrous turbid medium," *Appl. Opt.* **49**(5), 838–844 (2010).
10. H. H. He et al., "Two-dimensional backscattering Mueller matrix of sphere-cylinder scattering medium," *Opt. Lett.* **35**(14), 2323–2325 (2010).
11. S. Lu and R. Chipman, "Interpretation of Mueller matrices based on polar decomposition," *J. Opt. Soc. Am. A* **13**(5), 1106–1113 (1996).
12. N. Ghosh, M. F. G. Wood, and I. A. Vitkin, "Influence of the order of the constituent basis matrices on the Mueller matrix decomposition-derived polarization parameters in complex turbid media such as biological tissues," *Opt. Commun.* **283**(6), 1200–1208 (2010).
13. N. Ghosh and I. A. Vitkin, "Tissue polarimetry: concepts, challenges, applications, and outlook," *J. Biomed. Opt.* **16**(11), 110801 (2011).
14. N. Ghosh, M. F. G. Wood, and I. A. Vitkin, "Mueller matrix decomposition for extraction of individual polarization parameters from complex turbid media exhibiting multiple scattering, optical activity, and linear birefringence," *J. Biomed. Opt.* **13**(4), 044036 (2008).
15. N. Ghosh et al., "Mueller matrix decomposition for polarized light assessment of biological tissues," *J. Biophoton.* **2**(3), 145–156 (2009).
16. M. Dubreuil et al., "Mueller matrix polarimetry for improved liver fibrosis diagnosis," *Opt. Lett.* **37**(6), 1061–1063 (2012).
17. P. G. Ellingsen et al., "Quantitative characterization of articular cartilage using Mueller matrix imaging and multiphoton microscopy," *J. Biomed. Opt.* **16**(11), 116002 (2011).
18. S. Kumar et al., "Comparative study of differential matrix and extended polar decomposition formalisms for polarimetric characterization of complex tissue-like turbid media," *J. Biomed. Opt.* **17**(10), 105006 (2012).
19. S. Alali et al., "Optical assessment of tissue anisotropy in ex vivo distended rat bladders," *J. Biomed. Opt.* **17**(8), 086010 (2012).
20. X. Z. Wang, J. C. Lai, and Z. H. Li, "Polarization studies for backscattering of RBC suspensions based on Mueller matrix decomposition," *Opt. Express* **20**(18), 20771–20782 (2012).
21. A. Shuaib, X. Li, and G. Yao, "Transmission of polarized light in skeletal muscle," *J. Biomed. Opt.* **16**(2), 025001 (2011).
22. J. Ranasinghesagara and G. Yao, "Imaging 2D optical diffuse reflectance in skeletal muscle," *Opt. Express* **15**(7), 3998–4007 (2007).
23. H. H. He et al., "Application of sphere-cylinder scattering model to skeletal muscle," *Opt. Express* **18**(14), 15104–15112 (2010).
24. T. L. Yun et al., "Monte Carlo simulation of polarized photon scattering in anisotropic media," *Opt. Express* **17**(19), 16590–16602 (2009).
25. R. Liao et al., "Rotating linear polarization imaging technique for anisotropic tissues," *J. Biomed. Opt.* **15**(3), 036014 (2010).
26. N. Zeng et al., "Linear polarization difference imaging and its potential applications," *Appl. Opt.* **48**(35), 6734–6739 (2009).
27. B. D. Cameron et al., "Measurement and calculation of the two-dimensional backscattering Mueller matrix of a turbid medium," *Opt. Lett.* **23**(7), 485–487 (1998).

28. X. Li and G. Yao, "Mueller matrix decomposition of diffuse reflectance imaging in skeletal muscle," *Appl. Opt.* **48**(14), 2625–2631 (2009).
29. M. Ahmad et al., "Do different turbid media with matched bulk optical properties also exhibit similar polarization properties," *Biomed. Opt. Express* **2**(12), 3248–3258 (2011).
30. G. Anna et al., "Fully tunable active polarization imager for contrast enhancement and partial polarimetry," *Appl. Opt.* **51**(21), 3302–5309 (2012).
31. A. Pierangelo et al., "Ex vivo photometric and polarimetric multilayer characterization of human healthy colon by multispectral Mueller imaging," *J. Biomed. Opt.* **17**(6), 066009 (2012).
32. G. Anna, F. Goudail, and D. Dolfi, "Polarimetric target detection in the presence of spatially fluctuating Mueller matrices," *Opt. Lett.* **36**(23), 4590–4592 (2011).
33. G. Anna, F. Goudail, and D. Dolfi, "Optimal discrimination of multiple regions with an active polarimetric imager," *Opt. Express* **19**(25), 25367–25378 (2011).
34. A. Pierangelo et al., "Ex-vivo characterization of human colon cancer by Mueller polarimetric imaging," *Opt. Express* **19**(2), 1582–1593 (2011).
35. E. Du et al., "Two-dimensional backscattering Mueller matrix of sphere-cylinder birefringence media," *J. Biomed. Opt.* **17**(12), 126016 (2012).